

A hybrid discrete-continuum approach to model Turing pattern formation

*Original*

A hybrid discrete-continuum approach to model Turing pattern formation / Macfarlane, F. R.; Chaplain, M. A. J.; Lorenzi, T.. - In: MATHEMATICAL BIOSCIENCES AND ENGINEERING. - ISSN 1551-0018. - 17:6(2020), pp. 7442-7479. [10.3934/mbe.2020381]

*Availability:*

This version is available at: 11583/2870769 since: 2021-02-12T12:41:28Z

*Publisher:*

NLM (Medline)

*Published*

DOI:10.3934/mbe.2020381

*Terms of use:*

This article is made available under terms and conditions as specified in the corresponding bibliographic description in the repository

*Publisher copyright*

(Article begins on next page)

### 3.3. Numerical simulations

In this section, we carry out a systematic quantitative comparison between the results of numerical simulations of the hybrid model presented in Section 3.1 and numerical solutions of the corresponding continuum model given in Section 3.2, both in one and in two spatial dimensions. All simulations are performed in MATLAB and the final time of simulations is chosen such that the essential features of the pattern formation process are evident.

#### 3.3.1. Summary of the set-up of numerical simulations

We define the functions  $P$ ,  $Q$ ,  $\psi$ ,  $\phi_u$  and  $\phi_v$  as in the case of static domains. In more detail,  $P$  and  $Q$  are provided in definitions (2.19),  $\psi$  is defined via Eq (2.20), and  $\phi_u$  and  $\phi_v$  are given via either definitions (2.21) or definitions (2.22).

In all simulations, we let the initial spatial distributions of morphogens and cells be the numerical steady state distributions obtained in the case of static domains with  $\ell := 1$ , and we assume the domain to slowly grow linearly over time, that is,

$$\mathcal{L}(t) := 1 + 0.01 t. \quad (3.16)$$

Given the values of the parameters chosen to carry out numerical simulations of the IB model, we describe  $D_n$  and  $C_n$  via the definitions (2.23) so that conditions (2.16) are met. A complete description of the set-up of numerical simulations is given in Appendix C.

#### 3.3.2. Main results of numerical simulations

**Dynamics of the morphogens** The plots in the top rows of Figures 7 and 8 and in the Supplementary Figure D2 summarise the dynamics of the continuum concentrations of morphogens  $u(t, \hat{\mathbf{x}})$  and  $v(t, \hat{\mathbf{x}})$  obtained by solving numerically the system of PDEs (3.15) subject to zero-flux boundary conditions and with  $G(\hat{\mathbf{x}}, u, \mathcal{L})$  and  $G(\hat{\mathbf{x}}, v, \mathcal{L})$  defined via Eq (3.13), while the plots in the top rows of Figures 9 and 10 and in the Supplementary Figure D3 refer to the case where  $G(\hat{\mathbf{x}}, u, \mathcal{L})$  and  $G(\hat{\mathbf{x}}, v, \mathcal{L})$  are defined via Eq (3.14). Identical results hold for the discrete morphogen concentrations  $u_i^k$  and  $v_i^k$  obtained by solving the system of difference equations (3.2) (results not shown). These plots demonstrate that, when the spatial domain grows over time, a dynamical rescaling and repetition of the Turing pre-patterns observed in the case of static domains occurs—i.e., spots of high concentration repeatedly split symmetrically. In the case of uniform domain growth, such a self-similar process occurs throughout the whole domain, while in the case of apical growth the process takes place toward the growing edge of the domain.

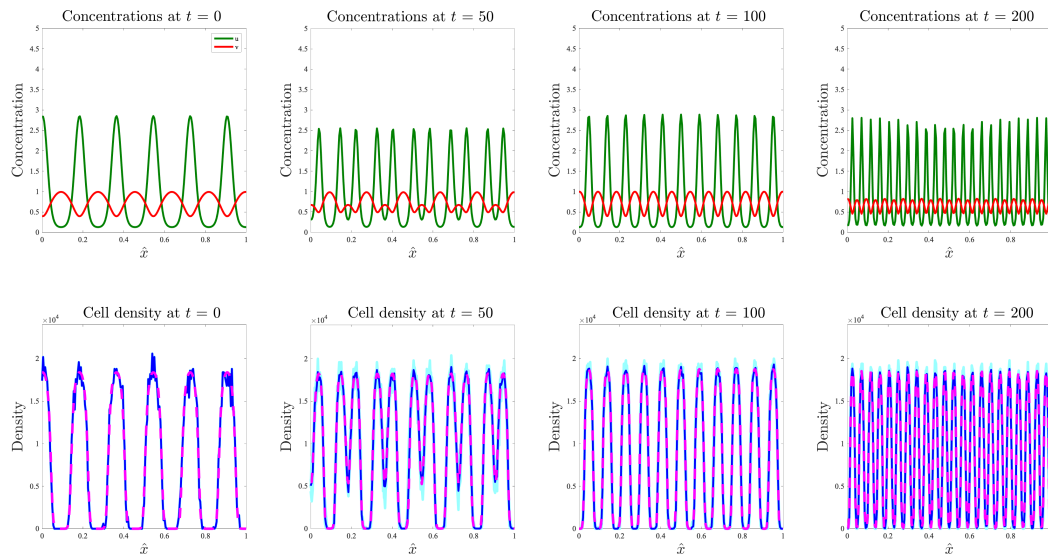


**Figure 7.** Results of numerical simulations on a one-dimensional uniformly growing domain in the presence of chemically-controlled cell proliferation. (Top row) Plots of the concentrations of morphogens at four consecutive time instants. The green lines highlight the concentration of activator  $u(t, \hat{x})$  and the red lines highlight the concentration of inhibitor  $v(t, \hat{x})$  obtained by solving numerically the system of PDEs (3.15) for  $d = 1$  subject to zero-flux boundary conditions, and complemented with the definitions (2.19), Eqs (3.13) and (3.16). (Bottom row) Comparison between the discrete cell density  $n_i^k$  obtained by averaging the results of computational simulations of the IB model (solid dark blue lines) and the continuum cell density  $n(t, \hat{x})$  obtained by solving numerically the PDE (3.12) for  $d = 1$  subject to zero-flux boundary conditions and complemented with Eqs (3.13) and (3.16) (pink dashed lines), at four consecutive time instants. Here,  $\eta = 0$ ,  $C_n = 0$ , and the functions  $\phi_u$  and  $\phi_v$  are given by definitions (2.21). We additionally set the initial cell density  $n_i^0 = 10^4$  for all  $i$ . The results from the IB model correspond to the average over five realisations of the underlying branching random walk, with the results from each realisation plotted in pale blue to demonstrate the robustness of the results obtained. A complete description of the set-up of numerical simulations is given in Appendix C.

**Dynamics of the cells** The plots in the bottom row of Figure 7 and the plots in Figure 11 summarise the dynamics of the cell density in the case where there is no chemotaxis, chemically-controlled cell proliferation occurs—i.e., when  $\eta = 0$ ,  $C_n = 0$ , and the functions  $\phi_u$  and  $\phi_v$  are given by definitions (2.21)—and the functions  $g_i(n_i^k, \mathcal{L}_k)$  and  $G(\hat{\mathbf{x}}, n, \mathcal{L})$  are defined via Eqs (3.3) and (3.13), respectively. On the other hand, the plots in the bottom row of Figure 9 and the plots in Figure 12 refer to the case where the functions  $g_i(n_i^k, \mathcal{L}_k)$  and  $G(\hat{\mathbf{x}}, n, \mathcal{L})$  are defined via Eqs (3.4) and (3.14). These plots indicate that, when the spatial domain grows over time, spots of high cell density stretch either throughout the domain (uniform growth) or at the growing edge (apical growth) before splitting. This process causes cell patterns to rescale and repeat across the domain at a smaller scale. These plots demonstrate also that there is a good quantitative match between the discrete cell density

$n_i^k$  given by Eq (2.1), with  $N_i^k$  obtained through computational simulations of the IB model, and the continuum cell density  $n(t, \hat{x})$  obtained by solving numerically the PDE (3.12) subject to zero-flux boundary conditions and complemented with either Eq (3.13) or Eq (3.14), both in one and in two spatial dimensions.

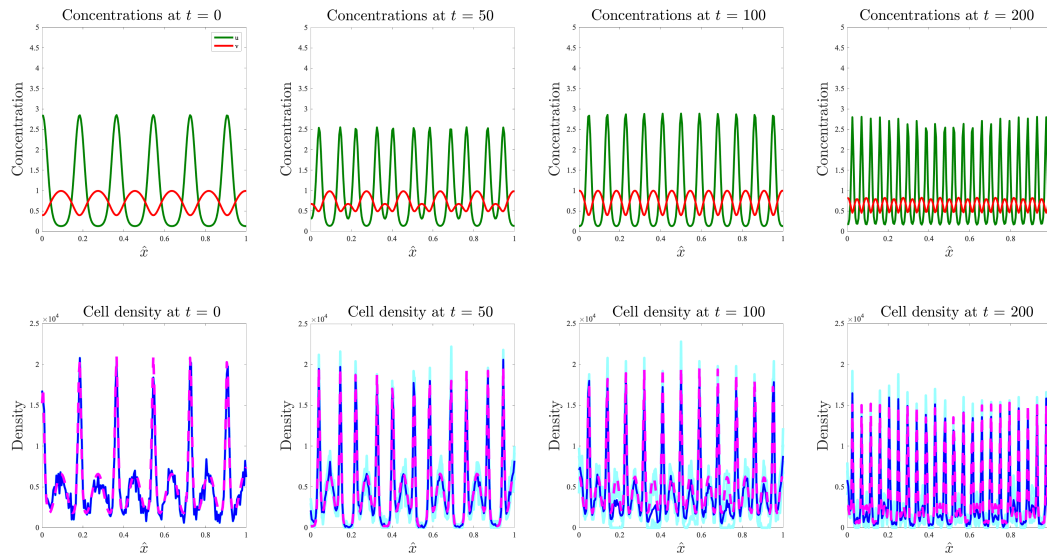


**Figure 8.** Results of numerical simulations on a one-dimensional uniformly growing domain in the presence of chemotaxis. (Top row) Plots of the concentrations of morphogens at four consecutive time instants. The green lines highlight the concentration of activator  $u(t, \hat{x})$  and the red lines highlight the concentration of inhibitor  $v(t, \hat{x})$  obtained by solving numerically the system of PDEs (3.15) for  $d = 1$  subject to zero-flux boundary conditions, and complemented with the definitions (2.19), Eqs (3.13) and (3.16). (Bottom row) Comparison between the discrete cell density  $n_i^k$  obtained by averaging the results of computational simulations of the IB model (solid dark blue lines) and the continuum cell density  $n(t, \hat{x})$  obtained by solving numerically the PDE (3.12) for  $d = 1$  subject to zero-flux boundary conditions and complemented with Eqs (3.13) and (3.16) (pink dashed lines), at four consecutive time instants. Here,  $\eta > 0$ ,  $C_n > 0$ , and the functions  $\phi_u$  and  $\phi_v$  are described through the definitions (2.22). We additionally set the initial cell density  $n_i^0 = 10^4$  for all  $i$ . The results from the IB model correspond to the average over five realisations of the underlying branching random walk, with the results from each realisation plotted in pale blue to demonstrate the robustness of the results obtained. A complete description of the set-up of numerical simulations is given in Appendix C.

Analogous considerations apply to the case where cell proliferation is not regulated by the morphogens and chemotactic movement of the cells up the concentration gradient of the activator occurs—i.e., when the functions  $\phi_u$  and  $\phi_v$  are described through the definitions (2.22),  $\eta > 0$  and  $C_n > 0$ —see the plots in the bottom row of Figure 8 along with the plots in Figure 13 and the plots in the bottom row of Figure 10 along with the plots in Figure 14.

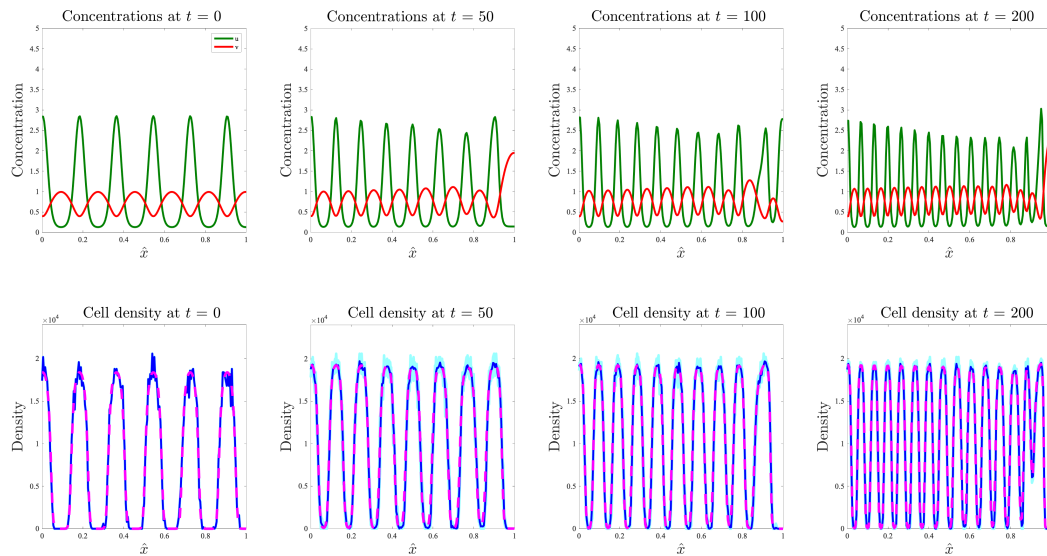


**Figure 9.** Results of numerical simulations on a one-dimensional apically growing domain in the presence of chemically-controlled cell proliferation. (Top row) Plots of the concentrations of morphogens at four consecutive time instants. The green lines highlight the concentration of activator  $u(t, \hat{x})$  and the red lines highlight the concentration of inhibitor  $v(t, \hat{x})$  obtained by solving numerically the system of PDEs (3.15) for  $d = 1$  subject to zero-flux boundary conditions, complemented with the definitions (2.19), Eqs (3.14) and (3.16). (Bottom row) Comparison between the discrete cell density  $n_i^k$  obtained by averaging the results of computational simulations of the IB model (solid dark blue lines) and the continuum cell density  $n(t, \hat{x})$  obtained by solving numerically the PDE (3.12) for  $d = 1$  subject to zero-flux boundary conditions and complemented with Eqs (3.14) and (3.16) (pink dashed lines), at four consecutive time instants. Here,  $\eta = 0$ ,  $C_n = 0$ , and the functions  $\phi_u$  and  $\phi_v$  are given by definitions (2.21). We additionally set the initial cell density  $n_i^0 = 10^4$  for all  $i$ . The results from the IB model correspond to the average over five realisations of the underlying branching random walk, with the results from each realisation plotted in pale blue to demonstrate the robustness of the results obtained. A complete description of the set-up of numerical simulations is given in Appendix C.

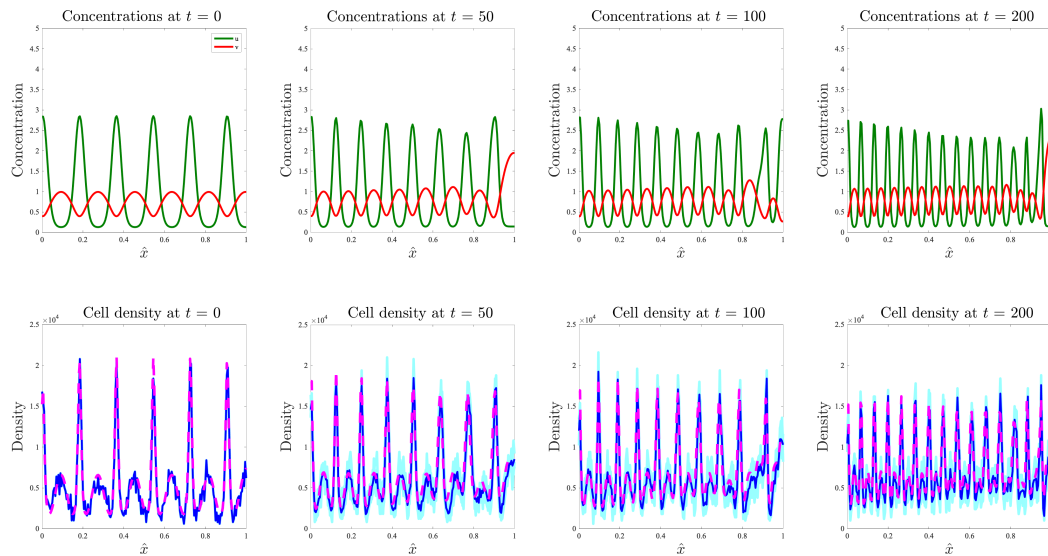


**Figure 10.** Results of numerical simulations on a one-dimensional apically growing domain in the presence of chemotaxis. (Top row) Plots of the concentrations of morphogens at four consecutive time instants. The green lines highlight the concentration of activator  $u(t, \hat{x})$  and the red lines highlight the concentration of inhibitor  $v(t, \hat{x})$  obtained by solving numerically the system of PDEs (3.15) for  $d = 1$  subject to zero-flux boundary conditions, complemented with the definitions (2.19), Eqs (3.14) and (3.16). (Bottom row) Comparison between the discrete cell density  $n_i^k$  obtained by averaging the results of computational simulations of the IB model (solid dark blue lines) and the continuum cell density  $n(t, \hat{x})$  obtained by solving numerically the PDE (3.12) for  $d = 1$  subject to zero-flux boundary conditions and complemented with Eqs (3.14) and (3.16) (pink dashed lines), at four consecutive time instants. Here,  $\eta > 0$ ,  $C_n > 0$ , and the functions  $\phi_u$  and  $\phi_v$  are described through the definitions (2.22). We additionally set the initial cell density  $n_i^0 = 10^4$  for all  $i$ . The results from the IB model correspond to the average over five realisations of the underlying branching random walk, with the results from each realisation plotted in pale blue to demonstrate the robustness of the results obtained. A complete description of the set-up of numerical simulations is given in Appendix C.

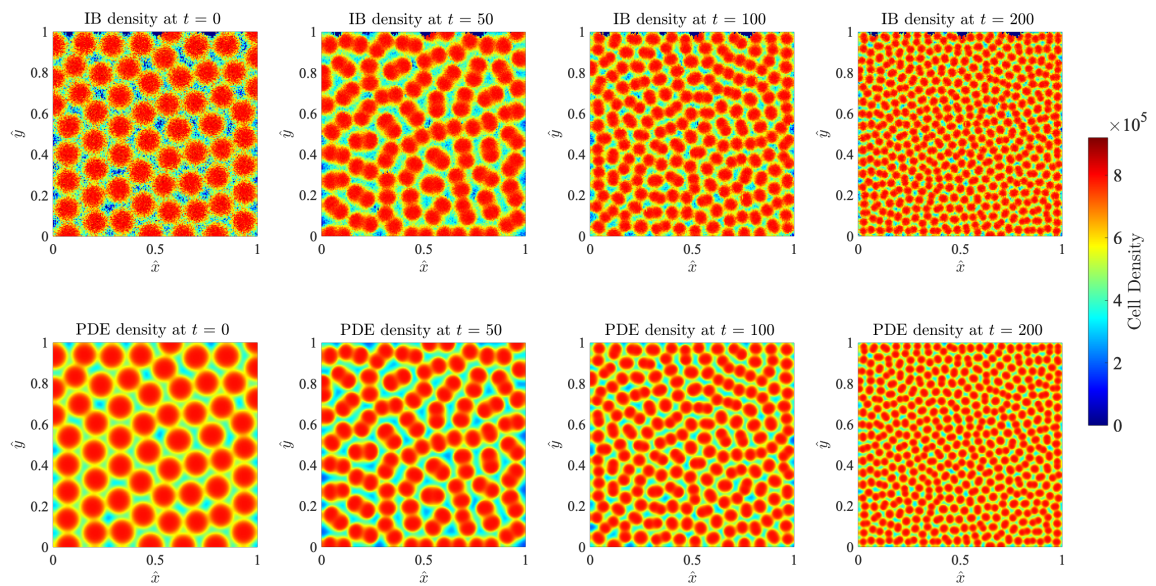


**Figure 11.** Results of numerical simulations on a two-dimensional uniformly growing domain in the presence of chemically-controlled cell proliferation. Comparison between the discrete cell density  $n_{\mathbf{i}}^k$  obtained by averaging the results of computational simulations of the IB model (top row) and the continuum cell density  $n(t, \hat{\mathbf{x}})$  obtained by solving numerically the PDE (3.12) for  $d = 2$  subject to zero-flux boundary conditions and complemented with Eqs (3.13) and (3.16) (bottom row), at four consecutive time instants. Here,  $\eta = 0$ ,  $C_n = 0$ , and the functions  $\phi_u$  and  $\phi_v$  are given by definitions (2.21). We additionally set the initial cell density  $n_{\mathbf{i}}^0 = 4 \times 10^5$  for all  $\mathbf{i}$ . The results from the IB model correspond to the average over five realisations of the underlying branching random walk. The plots of the corresponding morphogen concentrations are displayed in the Supplementary Figure D2. A complete description of the set-up of numerical simulations is given in Appendix C.

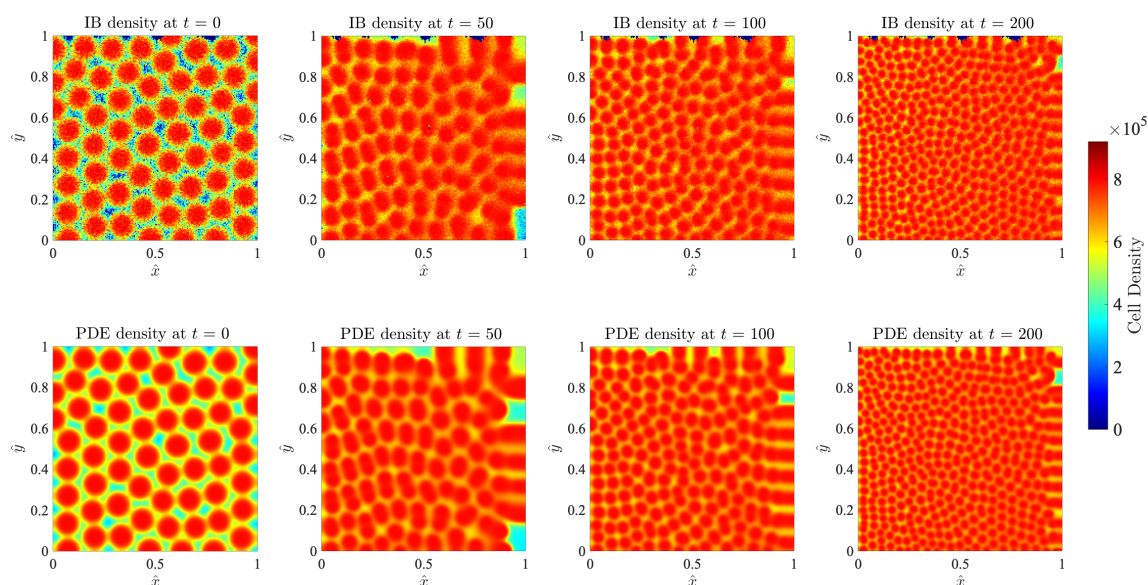


**Figure 12.** Results of numerical simulations on a two-dimensional apically growing domain in the presence of chemically-controlled cell proliferation. Comparison between the discrete cell density  $n_i^k$  obtained by averaging the results of computational simulations of the IB model (top row) and the continuum cell density  $n(t, \hat{\mathbf{x}})$  obtained by solving numerically the PDE (3.12) for  $d = 2$  subject to zero-flux boundary conditions and complemented with Eqs (3.14) and (3.16) (bottom row), at four consecutive time instants. Here,  $\eta = 0$ ,  $C_n = 0$ , and the functions  $\phi_u$  and  $\phi_v$  are given by definitions (2.21). We additionally set the initial cell density  $n_i^0 = 4 \times 10^5$  for all  $\mathbf{i}$ . The results from the IB model correspond to the average over five realisations of the underlying branching random walk. The plots of the corresponding morphogen concentrations are displayed in the Supplementary Figure D3. A complete description of the set-up of numerical simulations is given in Appendix C.

## 4. Conclusions and research perspectives

### 4.1. Conclusions

We have developed a hybrid discrete-continuum modelling framework that can be used to describe the formation of cellular patterns, specifically focusing on the Turing mechanism as the driving force behind the patterns. We used reaction-diffusion systems to describe the evolution of morphogens, which dictate the action of cells, while cell dynamics were described by stochastic IB models. We formally derived the deterministic continuum counterparts of the IB models, which were formulated as PDEs for the cell density, and compared the two modelling approaches through numerical simulations both in the case of stationary spatial domains and in the case of two types of growing domains, corresponding to uniform and apical growth. Numerical simulations demonstrated that in the case of sufficiently large cell numbers there was an excellent quantitative match between the spatial patterns produced by the stochastic IB model and its deterministic continuum counterpart.



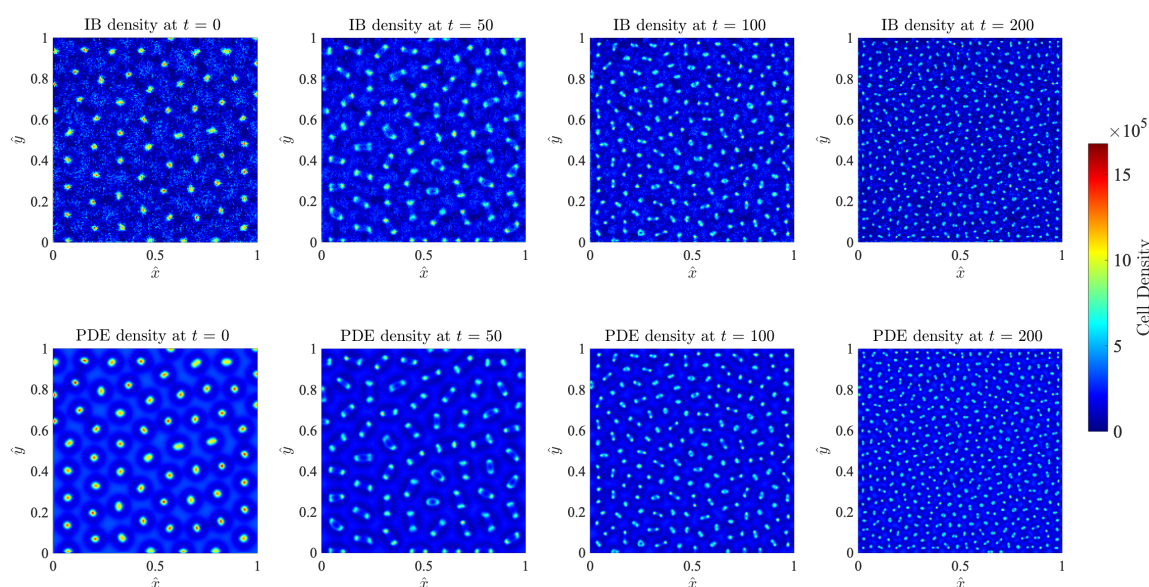


**Figure 13.** Results of numerical simulations on a two-dimensional uniformly growing domain in the presence of chemically-controlled cell proliferation. Comparison between the discrete cell density  $n_i^k$  obtained by averaging the results of computational simulations of the IB model (top row) and the continuum cell density  $n(t, \hat{\mathbf{x}})$  obtained by solving numerically the PDE (3.12) for  $d = 2$  subject to zero-flux boundary conditions and complemented with Eqs (3.13) and (3.16) (bottom row), at four consecutive time instants. Here,  $\eta > 0$ ,  $C_n > 0$ , and the functions  $\phi_u$  and  $\phi_v$  are described through the definitions (2.22). We additionally set the initial cell density  $n_i^0 = 4 \times 10^5$  for all  $\mathbf{i}$ . The results from the IB model correspond to the average over five realisations of the underlying branching random walk. The plots of the corresponding morphogen concentrations are displayed in the Supplementary Figure D2. A complete description of the set-up of numerical simulations is given in Appendix C.

Moreover, in the case of static domains, we also presented the results of numerical simulations showing that possible differences between the spatial patterns produced by the two modelling approaches could emerge in the regime of sufficiently low cell numbers. In fact, lower cell numbers correlated with both lower regularity of the cell density and demographic stochasticity, which may cause a reduction in the quality of the approximations employed in the formal derivation of the deterministic continuum model from the stochastic IB model. Hence, having both types of models available allows one to use IB models in the regime of low cells numbers—i.e., when stochastic effects associated with small cell population levels, which cannot be captured by PDE models, are particularly relevant—and then turn to their less computationally expensive PDE counterparts when large cell numbers need to be considered—i.e., when stochastic effects associated with small cell population levels are negligible.

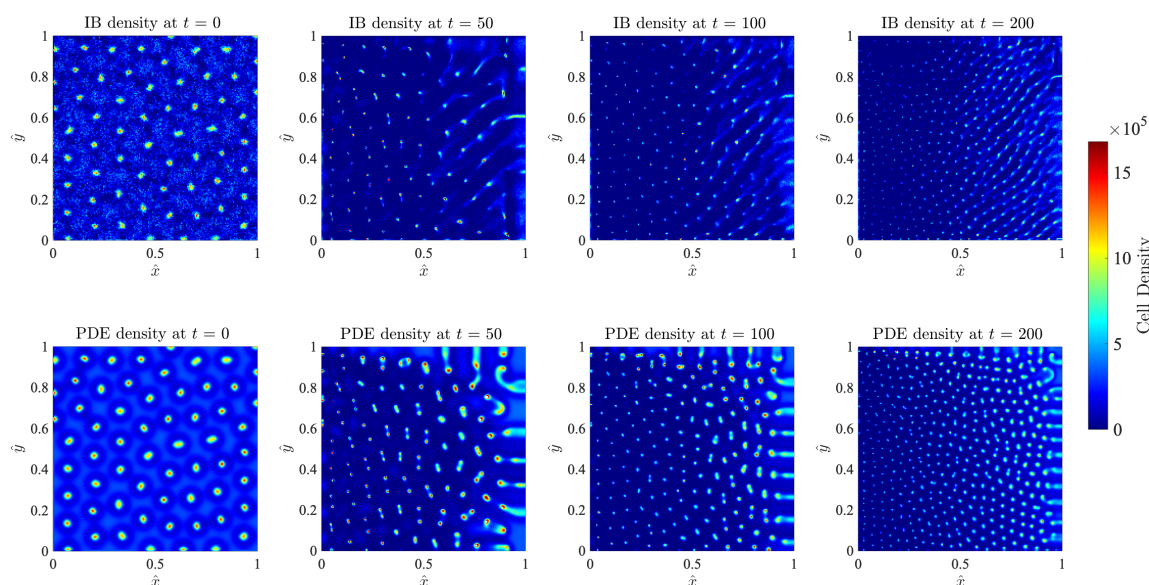


**Figure 14.** Results of numerical simulations on a two-dimensional apically growing domain in the presence of chemically-controlled cell proliferation. Comparison between the discrete cell density  $n_i^k$  obtained by averaging the results of computational simulations of the IB model (top row) and the continuum cell density  $n(t, \hat{\mathbf{x}})$  obtained by solving numerically the PDE (3.12) for  $d = 2$  subject to zero-flux boundary conditions and complemented with Eqs (3.14) and (3.16) (bottom row), at four consecutive time instants. Here,  $\eta > 0$ ,  $C_n > 0$ , and the functions  $\phi_u$  and  $\phi_v$  are described through the definitions (2.22). We additionally set the initial cell density  $n_i^0 = 4 \times 10^5$  for all  $\mathbf{i}$ . The results from the IB model correspond to the average over five realisations of the underlying branching random walk. The plots of the corresponding morphogen concentrations are displayed in the Supplementary Figure D3. A complete description of the set-up of numerical simulations is given in Appendix C.

#### 4.2. Research perspectives

There are a number of additional elements that would be relevant to incorporate into the modelling framework presented here in order to further broaden its spectrum of applications.

For instance, as was recognised by Turing himself, exogenous diffusing chemicals are not the only vehicle of coordination between cells. In particular, it is known that long range cell-cell interactions can be mediated by signal proteins produced by the cells themselves and also by mechanical forces between cells and components of the cellular microenvironment. For example, vascular endothelial growth factor signalling has been shown to control neural crest cell migration [79–81], and mechanical interactions between cells and the extra cellular matrix can control cell aggregation [82]. Moreover, cellular patterning leading to the emergence of spatial structures often requires the interplay between non-diffusible species, transcription factors and cell signalling—*viz.* the process underlying digit formation in tetrapods [83]. In this regard, it would be interesting to extend the modelling framework by allowing the cells to consume and/or produce chemicals required for successful coordination of their actions [84], and by incorporating more complex cellular processes

such as anoikis [85, 86] and cell deformation [87, 88]. In the situation where local production and/or consumption of the chemicals by the cells occurs, for particular cases such as those considered in [44], we would still expect it to be possible to derive an effective deterministic continuum limit of the IB model for the dynamics of the cells through formal procedures analogous to the one used here. However, there could also be cases in which PDE models derived using similar formal procedures might not be able to faithfully reproduce the dynamics of the branching random walk underlying the IB model, due to the interplay between stochastic effects and nonlinear dynamical interactions between the cells and the chemicals.

To date, only few biological systems have been demonstrated to satisfy the necessary conditions required for the formation of Turing pre-patterns via reaction-diffusion systems. Since mathematical models formulated as scalar integro-differential equations, whereby the formation of Turing-like patterns is governed by suitable integral kernels, have proven capable of faithfully reproduce a variety of pigmentation patterns in fish [27, 89], it would also be interesting to explore possible ways of integrating such alternative modelling strategies into our framework.

## Acknowledgments

MAJC gratefully acknowledges support of EPSRC Grant No. EP/N014642/1 (EPSRC Centre for Multiscale Soft Tissue Mechanics–With Application to Heart & Cancer).

## Conflict of interest

All authors declare no conflicts of interest in this paper.

## References

1. A. M. Turing, The chemical basis of morphogenesis, *Philos. Trans. R. Soc. Lond. B*, **237** (1952), 37–72.
2. A. Gierer and H. Meinhardt, A theory of biological pattern formation, *Kybernetik*, **12** (1972), 30–39.
3. H. Meinhardt, *Models of Biological Pattern Formation*, Academic Press, London, 1982.
4. J. D. Murray, A pre-pattern formation mechanism for animal coat markings, *J. Theor. Biol.*, **88** (1981), 161–199.
5. P. K. Maini and T. E. Woolley, The Turing model for biological pattern formation, in *The Dynamics of Biological Systems*, Springer, 2019, 189–204.
6. P. Arcuri and J. D. Murray, Pattern sensitivity to boundary and initial conditions in reaction-diffusion models, *J. Math. Biol.*, **24** (1986), 141–165.
7. M. A. J. Chaplain, M. Ganesh, and I. G. Graham, Spatio-temporal pattern formation on spherical surfaces: Numerical simulation and application to solid tumour growth, *J. Math. Biol.*, **42** (2001), 387–423.
8. E. J. Crampin, E. A. Gaffney, and P. K. Maini, Reaction and diffusion on growing domains: Scenarios for robust pattern formation, *Bull. Math. Biol.*, **61** (1999), 1093–1120.

9. E. J. Crampin, W. W. Hackborn, and P. K. Maini, Pattern formation in reaction-diffusion models with nonuniform domain growth, *Bull. Math. Biol.*, **64** (2002), 747–769.
10. S. Kondo and R. Asai, A reaction-diffusion wave on the skin of the marine angelfish *Pomacanthus*, *Nature*, **376** (1995), 765–768.
11. A. L. Krause, M. A. Ellis, and R. A. Van Gorder. Influence of curvature, growth, and anisotropy on the evolution of Turing patterns on growing manifolds, *Bull. Math. Biol.*, **81** (2019), 759–799.
12. A. L. Krause, V. Klika, T. E. Woolley, and E. A. Gaffney, From one pattern into another: Analysis of Turing patterns in heterogeneous domains via WKB, *J. R. Soc. Interface*, **17** (2020), 20190621.
13. P. K. Maini, T. E. Woolley, R. E. Baker, E. A. Gaffney, and S. S. Lee, Turing’s model for biological pattern formation and the robustness problem, *Interface Focus*, **2** (2012), 487–496.
14. A. Madzvamuse, A. H. W. Chung, and C. Venkataraman, Stability analysis and simulations of coupled bulk-surface reaction–diffusion systems, *Proc. R. Soc. A*, **471** (2015), 20140546.
15. A. Madzvamuse, A. J. Wathen, and P. K. Maini, A moving grid finite element method applied to a model biological pattern generator, *J. Comp. Phys.*, **190** (2003), 478–500.
16. K. J. Painter, P. K. Maini, and H. G. Othmer, Stripe formation in juvenile *Pomacanthus* explained by a generalized Turing mechanism with chemotaxis, *Proc. Nat. Acad. Sci.*, **96** (1999), 5549–5554.
17. S. S. Lee, E. A. Gaffney, and R. E. Baker, The dynamics of Turing patterns for morphogen-regulated growing domains with cellular response delays, *Bull. Math. Biol.*, **73** (2011), 2527–2551.
18. J. D. Murray, *Mathematical Biology: I. An Introduction*, volume 17. Springer Science & Business Media, 2007.
19. B. Ermentrout, Stripes or spots? Nonlinear effects in bifurcation of reaction-diffusion equations on the square, *Proc. R. Soc. A*, **434** (1991), 413–417.
20. H. Shoji, Y. Iwasa, and S. Kondo, Stripes, spots, or reversed spots in two-dimensional Turing systems, *J. Theor. Biol.*, **224** (2003), 339–350.
21. H. Meinhardt, Tailoring and coupling of reaction-diffusion systems to obtain reproducible complex pattern formation during development of the higher organisms, *Appl. Math. Comput.*, **32** (1989), 103–135.
22. R. Chaturvedi, C. Huang, B. Kazmierczak, T. Schneider, J. A. Izaguirre, T. Glimm, H. G. E. Hentschel, J. A. Glazier, S. A. Newman and M. S. Alber, On multiscale approaches to three-dimensional modelling of morphogenesis, *J. R. Soc. Interface*, **2** (2005), 237–253.
23. S. Christley, M. S. Alber and S. A. Newman, Patterns of mesenchymal condensation in a multiscale, discrete stochastic model, *PLoS Comput. Biol.*, **3** (2007), e76.
24. B. Duggan and J. Metzcar, Generating Turing-like patterns in an off-lattice agent based model: Handout, *Preprint*.
25. D. Karig, K. M. Martini, T. Lu, N. A. DeLateur, N. Goldenfeld, and R. Weiss, Stochastic Turing patterns in a synthetic bacterial population, *Proc. Nat. Acad. Sci.*, **115** (2018), 6572–6577.
26. M. A. Kiskowski, M. S. Alber, G. L. Thomas, J. A. Glazier, N. B. Bronstein, J. Pu and S. A. Newman, Interplay between activator–inhibitor coupling and cell-matrix adhesion in a cellular automaton model for chondrogenic patterning, *Dev. Biol.*, **271** (2004), 372–387.

27. S. Kondo, Turing pattern formation without diffusion, in *Conference on Computability in Europe*, Springer, 2012, 416–421.
28. J. Moreira and A. Deutsch, Pigment pattern formation in zebrafish during late larval stages: A model based on local interactions, *Dev. Dyn.*, **232** (2005), 33–42.
29. S. Okuda, T. Miura, Y. Inoue, T. Adachi, and M. Eiraku, Combining Turing and 3D vertex models reproduces autonomous multicellular morphogenesis with undulation, tubulation, and branching, *Sci. Rep.*, **8** (2018), 1–15.
30. A. Volkening and B. Sandstede, Modelling stripe formation in zebrafish: An agent-based approach, *J. R. Soc. Interface*, **12** (2015), 20150812.
31. C. M. Glen, M. L. Kemp, and E. O. Voit, Agent-based modeling of morphogenetic systems: Advantages and challenges, *PLoS Comp. Biol.*, **15** (2019), e1006577.
32. J. A. Izaguirre, R. Chaturvedi, C. Huang, T. Cickovski, J. Coffland, G. Thomas, G. Forgacs, M. Alber, G. Hentschel, S. A. Newman, et al, CompuCell, a multi-model framework for simulation of morphogenesis, *Bioinformatics*, **20** (2004), 1129–1137.
33. T. M. Cickovski, C. Huang, R. Chaturvedi, T. Glimm, H. G. E. Hentschel, M. S. Alber, J. A. Glazier, S. A. Newman, and J. A. Izaguirre, A framework for three-dimensional simulation of morphogenesis, *Trans. Comput. Biol. Bioinform.*, **2** (2005), 273–288.
34. B. D. Hughes, *Random walks and random environments: Random walks*, vol. 1, Oxford University Press, 1995.
35. T. Hillen and H. G. Othmer, The diffusion limit of transport equations derived from velocity-jump processes, *SIAM J. Appl. Math.*, **61** (2000), 751–775.
36. T. Hillen and K. J. Painter, A user’s guide to PDE models for chemotaxis, *J. Math. Biol.*, **58** (2009), 183.
37. H. G. Othmer, S. R. Dunbar and W. Alt, Models of dispersal in biological systems, *J. Math. Biol.*, **26** (1988), 263–298.
38. K. J. Painter and T. Hillen, Volume-filling and quorum-sensing in models for chemosensitive movement, *Can. Appl. Math. Quart.*, **10**. (2002), 501–543.
39. K. J. Painter and J. A. Sherratt, Modelling the movement of interacting cell populations, *J. Theor. Biol.*, **225** (2003), 327–339.
40. W. Alt, Biased random walk models for chemotaxis and related diffusion approximations, *J. Math. Biol.*, **9** (1980), 147–177.
41. M. Burger, P. Markowich and J.-F. Pietschmann, Continuous limit of a crowd motion and herding model: analysis and numerical simulations, *Kinet. Relat. Models*, **4** (2011), 1025–1047.
42. A. Stevens, The derivation of chemotaxis equations as limit dynamics of moderately interacting stochastic many-particle systems, *SIAM J. Appl. Math.*, **61** (2000), 183–212.
43. A. Stevens and H. G. Othmer, Aggregation, blowup, and collapse: the abc’s of taxis in reinforced random walks, *SIAM J. Appl. Math.*, **57** (1997), 1044–1081.
44. F. Bubba, T. Lorenzi, and F. R. Macfarlane, From a discrete model of chemotaxis with volume-filling to a generalized patlak–keller–segel model, *Proc. R. Soc. A*, **476** (2020), 20190871.
45. N. Champagnat and S. Méléard, Invasion and adaptive evolution for individual-based spatially structured populations, *J. Math. Biol.*, **55** (2007), 147.

46. M. A. J. Chaplain, T. Lorenzi and F. R. Macfarlane, Bridging the gap between individual-based and continuum models of growing cell populations, *J. Math. Biol.*, **80** (2020), 342–371.
47. M. Inoue, Derivation of a porous medium equation from many markovian particles and the propagation of chaos, *Hiroshima Math. J.*, **21** (1991), 85–110.
48. K. Oelschläger, On the derivation of reaction-diffusion equations as limit dynamics of systems of moderately interacting stochastic processes, *Probab. Theory Relat. Fields*, **82** (1989), 565–586.
49. H. G. Othmer and T. Hillen, The diffusion limit of transport equations II: Chemotaxis equations, *SIAM J. Appl. Math.*, **62** (2002), 1222–1250.
50. C. J. Penington, B. D. Hughes and K. A. Landman, Building macroscale models from microscale probabilistic models: A general probabilistic approach for nonlinear diffusion and multispecies phenomena, *Phys. Rev. E*, **84** (2011), 041120.
51. C. J. Penington, B. D. Hughes and K. A. Landman, Interacting motile agents: Taking a mean-field approach beyond monomers and nearest-neighbor steps, *Phys. Rev. E*, **89** (2014), 032714.
52. R. E. Baker, A. Parker and M. J. Simpson, A free boundary model of epithelial dynamics, *J. Theor. Biol.*, **481** (2019), 61–74.
53. H. M. Byrne and D. Drasdo, Individual-based and continuum models of growing cell populations: A comparison, *J. Math. Biol.*, **58** (2009), 657.
54. T. Lorenzi, P. J. Murray and M. Ptashnyk, From individual-based mechanical models of multicellular systems to free-boundary problems, *Interface Free Bound.*, **22** (2020), 205–244.
55. S. Motsch and D. Peurichard, From short-range repulsion to hele-shaw problem in a model of tumor growth, *J. Math. Biol.*, **76** (2018), 205–234.
56. P. J. Murray, C. M. Edwards, M. J. Tindall and P. K. Maini, From a discrete to a continuum model of cell dynamics in one dimension, *Phys. Rev. E*, **80** (2009), 031912.
57. P. J. Murray, C. M. Edwards, M. J. Tindall and P. K. Maini, Classifying general nonlinear force laws in cell-based models via the continuum limit, *Phys. Rev. E*, **85** (2012), 021921.
58. K. Oelschläger, Large systems of interacting particles and the porous medium equation, *J. Diff. equation.*, **88** (1990), 294–346.
59. B. J. Binder and K. A. Landman, Exclusion processes on a growing domain, *J. Theor. Biol.*, **259** (2009), 541–551.
60. L. Dyson, P. K. Maini and R. E. Baker, Macroscopic limits of individual-based models for motile cell populations with volume exclusion, *Phys. Rev. E*, **86** (2012), 031903.
61. A. E. Fernando, K. A. Landman and M. J. Simpson, Nonlinear diffusion and exclusion processes with contact interactions, *Phys. Rev. E*, **81** (2010), 011903.
62. S. T. Johnston, R. E. Baker, D. S. McElwain and M. J. Simpson, Co-operation, competition and crowding: a discrete framework linking allee kinetics, nonlinear diffusion, shocks and sharp-fronted travelling waves, *Sci. Rep.*, **7** (2017), 42134.
63. S. T. Johnston, M. J. Simpson and R. E. Baker, Mean-field descriptions of collective migration with strong adhesion, *Phys. Rev. E*, **85** (2012), 051922.
64. K. A. Landman and A. E. Fernando, Myopic random walkers and exclusion processes: Single and multispecies, *Phys. A Stat. Mech. Appl.*, **390** (2011), 3742–3753.
65. P. M. Lushnikov, N. Chen and M. Alber, Macroscopic dynamics of biological cells interacting via chemotaxis and direct contact, *Phys. Rev. E*, **78** (2008), 061904.